High temperature deformation of polycrystalline C40 Mo(Si,Al)<inf>2</inf>

Materials Science & Engineering A 849 (2022) 143387

Contents lists available at ScienceDirect

Materials Science & Engineering A

journal homepage: www.elsevier.com/locate/msea

High temperature deformation of polycrystalline C40 $Mo(Si,Al)_2$

Aina Edgren [a,b], Erik Ström [b], Ren Qiu [a], Lars Frisk [c], Farid Akhtar [c], Magnus Hörnqvist Colliander [a,*]

[a] Chalmers University of Technology, Gothenburg, SE-41296, Sweden
[b] Kanthal AB, Hallstahammar, SE-73427, Sweden
[c] Luleå University of Technology, Luleå, SE-97187, Sweden

ARTICLE INFO

Keywords:
$Mo(Si,Al)_2$
Ceramics
High temperature compression
Electron backscatter diffraction
Dynamic recrystallization
Low angle grain boundaries

ABSTRACT

Polycrystalline $Mo(Si,Al)_2$ with C40 crystal structure was deformed in compression with a strain rate of 10^{-4} s^{-1} at 1300 °C. The specimens were deformed to a strain of 10%–15% and showed maximum stresses around 150 MPa prior to pronounced softening. No crack formation or significant increase in porosity could be observed. Post-test microstructure analysis revealed that the material was inhomogeneously deformed on both inter- and intragranular levels. Dynamic recrystallization occurred alongside low angle grain boundary formation in highly deformed grains. Furthermore, complex intragranular deformation fields suggest that slip systems other than $\langle 2\bar{1}\bar{1}0\rangle[0001]$ may be active during deformation.

1. Introduction

Electrification of industrial heating processes holds great promise for reducing CO_2 emissions as it allows the use of renewable and sustainable energy sources instead of combustion of fossil fuels. A large part of the emissions from fossil based heating arise during processes at very high temperatures (>1000 °C) [1], and enabling electrification of such processes is therefore critically important. However, the electrification of high power heating processes will require up-scaling from the kW range, for which most high temperature electric heating solutions are developed, to MWs. In the case of indirect resistive heating, which is a mature technology with large potential, high efficiency and low risk, this translates to heating elements with larger dimensions. Increased dimensions in turn increase the gravitational forces on the elements, particularly in combination with horizontal element mounting associated with ensuring uniform temperature distributions in large furnaces. It is therefore expected that, in addition to the traditionally life-limiting oxidation resistance which has received significant attention [2–5], the mechanical properties of the heating elements will have a larger influence on the performance and design space compared to the case in present applications.

In this study we address the lack of knowledge regarding mechanical behaviour of one ceramic candidate material for heating elements in high temperature industrial heating: $Mo(Si,Al)_2$. It has a high melting point, high resistivity, low density, resistance to pesting and excellent corrosion resistance in both oxidizing and reducing environments [2–5]. The latter is important for many industrial processes and clearly differentiates $Mo(Si,Al)_2$ from the more traditional ceramic heating elements made from $MoSi_2$, and has led to the preferred use of $Mo(Si,Al)_2$ heating elements in more demanding atmospheres.

$Mo(Si,Al)_2$ possesses a hexagonal C40 crystal structure [2,6]. This is a result of a significant amount of Al substituting for Si in $MoSi_2$ leading to a transition from the tetragonal $C11_b$ structure to C40 [6,7]. While the oxidation of C40 $Mo(Si,Al)_2$ has been extensively studied in recent years [2–5], the knowledge regarding the high temperature mechanical properties is still lacking. Studies of single crystals have shown that there is only one active slip system, $\langle 2\bar{1}\bar{1}0\rangle(0001)$ [6], which is the same system as observed in other C40 structured transition metal silicides such as $NbSi_2$, VSi_2, $CrSi_2$ and $TaSi_2$ [8–12]. The ductile to brittle transition temperature (DBTT) is high, around 1100 °C (0.6 T/T_m) for $Mo(Si,Al)_2$ single crystals [6,12,13], presumably due to deformation through the synchroshear mechanism [6]. The only available studies of polycrystalline $Mo(Si,Al)_2$ [13,14], which in turn is the only single phase C40 silicide for which polycrystals have been tested, have shown high temperature strength levels similar to $C11_b$ $MoSi_2$, DBTT around 1250 °C and fracture strains exceeding 20% above the DBTT. The large ductility of the polycrystalline material is interesting considering the presence of a single active slip system below 1500 °C [6,12], which does not allow fulfilment of the von Mises criterion.

Notably, no stress–strain curves or microstructure investigations were reported in Refs. [13,14], and the specifics regarding the deformation behaviour of polycrystalline $Mo(Si,Al)_2$ remains largely unknown. In the present investigation we perform compression testing

* Corresponding author.
E-mail address: magnus.colliander@chalmers.se (M. Hörnqvist Colliander).

https://doi.org/10.1016/j.msea.2022.143387
Received 8 March 2022; Received in revised form 27 May 2022; Accepted 28 May 2022
Available online 8 June 2022

of $Mo(Si,Al)_2$ polycrystals at 1300 °C, and report similar strength levels as previous studies, but significant softening after yielding. We perform detailed microstructural investigations of the undeformed and deformed material and show that recovery occurs through formation of low angle grain boundaries (LAGBs) and dynamic recrystallization (DRX). Examination of the plastic strain distribution between and within grains further suggests that there may be additional slip systems activated due to the complex stress states encountered in the grains due to strain compatibility in a deforming polycrystal.

2. Materials and methods

2.1. Material

Polycrystalline $Mo(Si,Al)_2$ was prepared by dry mixing of elemental Mo (99.9% purity, Cerac Inc.), Si (99.99% purity, Wacker) and Al (99.5% purity, GoodFellow) powders in a Mo-lined ball mill with Mo balls. The powder mixture was heated to initiate a self-propagating reaction in which $Mo(Si,Al)_2$ (as well as small amounts of $Mo_5(Si,Al)_3$ and Al_2O_3) was formed. The reaction product was milled and compacted to rods using a cold isostatic press (CIP, EPSI) operating at 2000 bar, prior to sintering in H_2 gas in a tube furnace (1 h at 1650 °C, ramp time from room temperature was 5 h). The as-sintered material had a density of 5.75 g/cm^3 (96% of theoretical density). The chemical composition of the sintered rod, measured using inductively coupled plasma mass spectrometry (ICP-MS), was 14.6 wt% Al, 20.1 wt% Si, 2.1 wt% Al_2O_3, 63.2 wt% Mo and 0.04 wt% Fe. Polycrystalline $MoSi_2$ (grain size 4 μm, 97 vol. %, $MoSi_2$ and small amounts of SiO_2 and Mo_5Si_3) was synthesized using the same procedure as described above for $Mo(Si,Al)_2$. This material was used for validation of the test method as it allowed direct comparison with previously reported tests of similar materials.

2.2. Materials characterization

The as-sintered rod was cut along the rod-axis, see Fig. 1(a), ground using SiC paper and polished using diamond suspension (down to 1 μm) and colloidal silica. The cross-section was characterized using scanning electron microscopy (SEM) imaging, energy-dispersive X-ray spectroscopy (EDS), electron backscatter diffraction (EBSD) as well as X-ray diffraction (XRD). For the SEM imaging and EDS, an FEI Quanta 200 FEG ESEM at an accelerating voltage was 20 kV was used. The EBSD data was obtained using a Tescan GAIA3 system, with an accelerating voltage of 15 kV. AZtec software by Oxford Instruments was used for both EDS and EBSD acquisition and analysis. The EBSD data were further analysed using the Channel 5 software by Oxford Instruments. XRD was performed using a Bruker D8 Advance equipped with a Cu-anode. Thin foil sample for scanning transmission electron microscopy (STEM) was prepared by standard lift-out method using an FEI Versa 3D focused ion beam (FIB)-SEM instrument equipped with an Omniprobe manipulator. STEM bight field (BF) characterization was carried out using an FEI Titan 80–300 instrument operated at 300 keV. EBSD was also performed on the lift-out foil sample.

2.3. Compression testing

The as-sintered $Mo(Si,Al)_2$ rods were ground to a diameter of 8 mm and cut into 12 mm long cylindrical specimens for compression testing. The specimens were tested with a strain rate of 10^{-4} s^{-1} at 1300 °C using a Gleeble 3800 thermomechanical simulator. Graphite foils and Ni-paste were used between the specimen and the anvils to minimize friction and ensure good electrical contact. As direct attachment of thermocouples internally or at the surface was not possible, the temperature was measured using a pyrometer. Al_2O_3 readily forms at the low vacuum levels employed here (10^{-2} mbar), and the samples were therefore tightly wrapped with a thin and flexible graphite foil. In this way, the emissivity of the surface did not change during compression testing. The constant emissivity, as well as the accuracy of the pyrometer, was verified using dummy steel samples with both welded thermocouples and graphite foil which were heated and held at different temperatures. It was shown that the temperature measured by the pyrometer did not deviate more than 4 °C above, or 8 °C below, the temperature measured by the thermocouple. Compression of a $MoSi_2$ sample at 1300 °C was used to validate the set-up, and the results agreed well with literature reports for the same test conditions (temperature and strain rate) and grain size. The maximum stress was of 101 MPa at a nominal strain of 7%, compared to 94 MPa and 5% reported by Mitra et al. [15]. During testing the $Mo(Si,Al)_2$ test specimens were heated to 1300 °C at a rate of 50 °C min^{-1} and held for 30 s to stabilize the temperature before deformation. Compression to a nominal strain of 10%–15% was performed in stroke control, which provided the most stable control mode. The displacement was measured using the L-Gauge, and the displacement signal will therefore contain contributions from compliance of the anvils and other parts of the system, apart from the deformation of the sample. Nevertheless, L-Gauge measures the displacement closer to the sample compared to the stroke, hence, the contribution from the system should be smaller compared to the case for the stroke signal.

Table 1
Chemical composition (at. %) and phase fractions (vol. %) in as-sintered material.

Phase	Crystal structure	Phase fraction	Mo	Si	Al	O
$Mo(Si,Al)_2$	C40 (hexagonal)	94.2	32.4	36.6	28.8	2.3
$Mo_5(Si,Al)_3$	$D8_m$ (tetragonal)	3.0	57.2	32.6	7.3	2.8
Al_2O_3	$D5_1$ (hexagonal)	1.7	0.8	1.7	39.6	58.0
Pores	–	1.1	–	–	–	–

3. Results

3.1. Microstructure of as-sintered material

The material consisted of three different phases, $Mo(Si,Al)_2$ (C40 structure), $Mo_5(Si,Al)_3$ ($D8_m$), and α-Al_2O_3, as well as pores. A back-scattered electron (BSE) micrograph, an EBSD phase map and an XRD diffractogram of the material are shown in Fig. 1. The chemical composition (determined using EDS) and volume fraction of the phases can be seen in Table 1. The O content in $Mo(Si,Al)_2$ and $Mo_5(Si,Al)_3$ is probably due nano-sized alumina particles dispersed in the two phases. Such particles were found both in this study and have been reported for a similar material by Ingemarsson et al. [2–4]. Small amounts of Mo and Si, probably traces from the synthesis reaction and/or due to large interaction volume in SEM, have been found in Al_2O_3. The phase fractions and porosity were determined from image analysis of BSE and SE images. Due to the low volume fractions of $Mo_5(Si,Al)_3$ and Al_2O_3, the analysis is from now on limited to $Mo(Si,Al)_2$, unless otherwise stated.

The grain size was measured using EBSD, with grain boundaries being defined by a misorientation of 10°. Some grains (which based on size, shape and EDS data are suggested to be $Mo(Si,Al)_2$) were difficult to index using EBSD even though the electron back-scattered patterns (EBSP), were clear and belonged to a hexagonal unit cell. Small areas inside such grains were nevertheless indexed resulting in identification of small, individual grains by the software algorithm (even when using reasonable minimum pixel number for grain definition), which resulted in a bimodal grain size distribution with one peak close to zero and another above 20 μm. The EBSD data was therefore cleaned by manually removing such grains. Removing the small grains instead of performing iterative expansion of indexed areas was chosen as the latter also expanded the neighbouring grains into the unindexed area, which was judged to result in larger errors compared to removal of the problematic grains. The removed regions were coloured black in the EBSD maps. After cleaning, the average grain size was 23 μm.

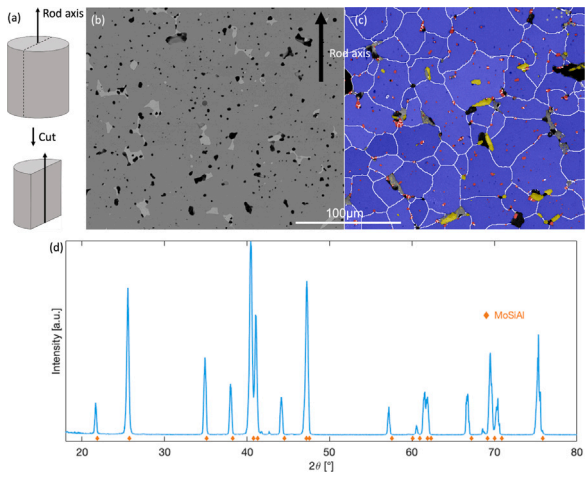

Fig. 1. (a) Cut of rod for microscopy study. Microstructure of the as-sintered $Mo(Si,Al)_2$ sample: (b) BSE image, and (c) EBSD map (blue = $Mo(Si,Al)_2$, yellow = $Mo_5(Si,Al)_3$ and red = Al_2O_3, black = manually removed $Mo(Si,Al)_2$, grey = non-indexed $Mo_5(Si,Al)_3$). (d) XRD pattern. The slight shift in peak position in (d) is due to small differences in chemical composition of $Mo(Si,Al)_2$ being analysed and the $Mo(Si,Al)_2$ material which the XRD card was based on (PDF 00-057-0374). (For interpretation of the references to colour in this figure legend, the reader is referred to the web version of this article.)

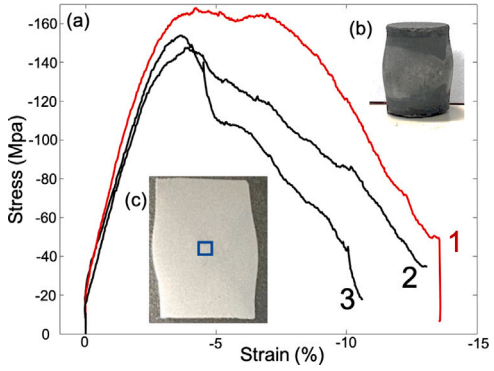

Fig. 2. (a) Stress–strain curves from the three compression tests. (b) Specimen 1 after deformation. (c) Cross-section of specimen 1 where the square indicates the position of the EBSD measurements.

3.2. Deformation behaviour

Three polycrystalline $Mo(Si,Al)_2$ specimens were successfully compressed at 1300 °C and the engineering stress–strain curves are shown in Fig. 2(a). Due to friction between the specimen and the anvils and the inhomogeneous temperature distribution induced by the Gleeble (heat conduction through the anvils leads to lower temperature closer to the ends compared to the centre [16–18]), the specimens become barrel-shaped during deformation, see Fig. 2(b) and (c). Note that the pyrometer was centred on the sample gauge length to measure the temperature where the plastic deformation is concentrated. Up to the onset of plastic deformation the stress is expected to be reasonably accurate, however, as the variation in cross-section along the sample due to barrelling increases with plastic deformation, the stresses and strains calculated from force and displacement become increasingly inaccurate after yielding. The measured strains also contain errors due to the origin of the displacement signal (the L-Gauge) and the deformation of the graphite films, Ni paste and even WC-Co anvils, which do deform to a certain degree at 1300 °C. The stresses and strains in Fig. 2 should therefore be taken as qualitative rather than quantitative.

The linear increase in stress seen in the first part of the stress–strain curves in Fig. 2 corresponds to the elastic region of deformation. However, due to the influence of compliance of parts other than the tested specimen, the slope in the linear region does not correspond to the Young's modulus. The curves deviate from linearity at stresses in the range 120–140 MPa, which indicates onset of plasticity. This confirms that the material has been tested above its DBTT temperature, which has been reported to be around 1250 °C for polycrystalline C40 $Mo(Si,Al)_2$ [13,14]. After limited hardening the samples experience a maximum in the stress response at around 4% strain, followed by softening down to 20–40 MPa. The maximum stress values are observed to be in the range of 148 and 168 MPa (average: 157 MPa). Hagihara et al. [14] and Umakoshi et al. [13] reported a yield stress of about 156 MPa for polycrystalline $Mo(Si,Al)_2$ at 1300 °C, which is very close to the maximum stress reported in this study. While there were no reports on how the yield stress was defined, the yield stress and the maximum stress should be rather close due to the limited work hardening seen in Fig. 2 and reported for polycrystalline $MoSi_2$ compression tested at the same temperature and strain rate [19]. The pronounced stress decrease in case of $Mo(Si,Al)_2$ in the present study, indicates that extensive recovery and/or activation of additional deformation mechanisms is taking place, in particular since the increasing area in the specimen centre leads to an overestimation of the stresses calculated based on assumptions of homogeneous plastic deformation. Such extent of softening was not observed by Mitra et al. for polycrystalline $MoSi_2$ [19] under the same deformation conditions. No compression curves or discussion of the stress response regarding the polycrystalline $Mo(Si,Al)_2$ was provided in Refs. [13,14] so the present results cannot be compared to these reports in more detail.

3.3. Microstructure of deformed specimen

After deformation, the specimen denoted 1 in Fig. 2 was selected for microstructure analysis using EBSD. The specimen was cut along the compression axis (which is the same as the rod axis in the as-sintered material) and the cross-section was ground and polished similar to the as-sintered material. From the centre region (indicated by the square in Fig. 2(c)) two EBSD maps (having the size of 400 × 400 µm and 450 × 300 µm) were obtained for better statistics. In total, the two maps contained 975 $Mo(Si,Al)_2$ grains. All histograms and plots presented in the following sections are based on these grains.

The microstructure of the tested specimen, in terms of an EBSD phase map, is shown in Fig. 3(a). Fig. 3(b) indicates that the major axis of ellipses fitted to the grains have become preferentially aligned perpendicular to the loading direction compared to the as-sintered material, where the angles are uniformly distributed. This suggests a "flattening" of the grains during compression, as would be expected during plastic deformation. The amount of porosity increased only slightly, from 1.1% in the undeformed material to 3.2% after compression, and no cracking could be observed. This clearly shows that polycrystalline $Mo(Si,Al)_2$ readily deforms plastically in compression at 1300 °C, without extensive formation of defects.

Further effects of plastic deformation can be seen in the increased intragranular lattice rotations, visualized by increased grain orientation spread (GOS, the average misorientation between each pixel in the grain and the average orientation of the grain) after deformation, compare Figs. 4(a) and (b), and in the histogram of the logarithm of the GOS shown in Fig. 4(c). Since lattice rotation is produced by geometrically necessary dislocations (GNDs), the increased GOS values indicate increasing GND densities. Also observed from the EBSD maps is that the microstructure has become finer due to deformation, which is confirmed in the grain size distribution shown in Fig. 4(d). Furthermore, the large grains in the deformed material have higher GOS values than the smaller grains, while the GOS is similar for all grain sizes in the undeformed material (Fig. 4(e)). The presence of small undeformed grains after compression suggests that dynamic recrystallization (DRX), is operating under the present deformation conditions, which could be

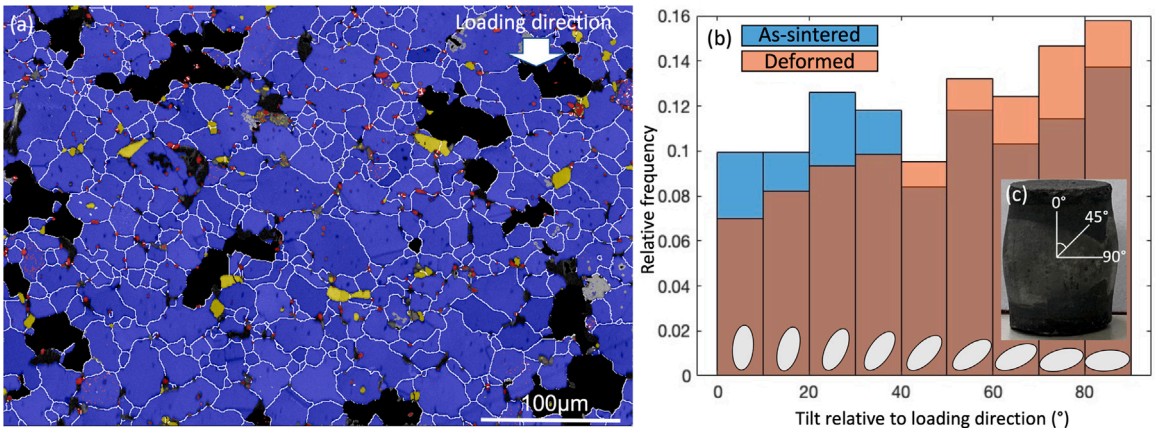

Fig. 3. (a) EBSD phase map of deformed specimen; (b) Histogram showing the relative frequency of the tilt of major grain axis of ellipses fitted to the grains relative the loading direction; (c) A deformed specimen showing the definition of the tilt angle with respect to the compression axis. The grey ellipses in (b) schematically show the tilt of each bin.

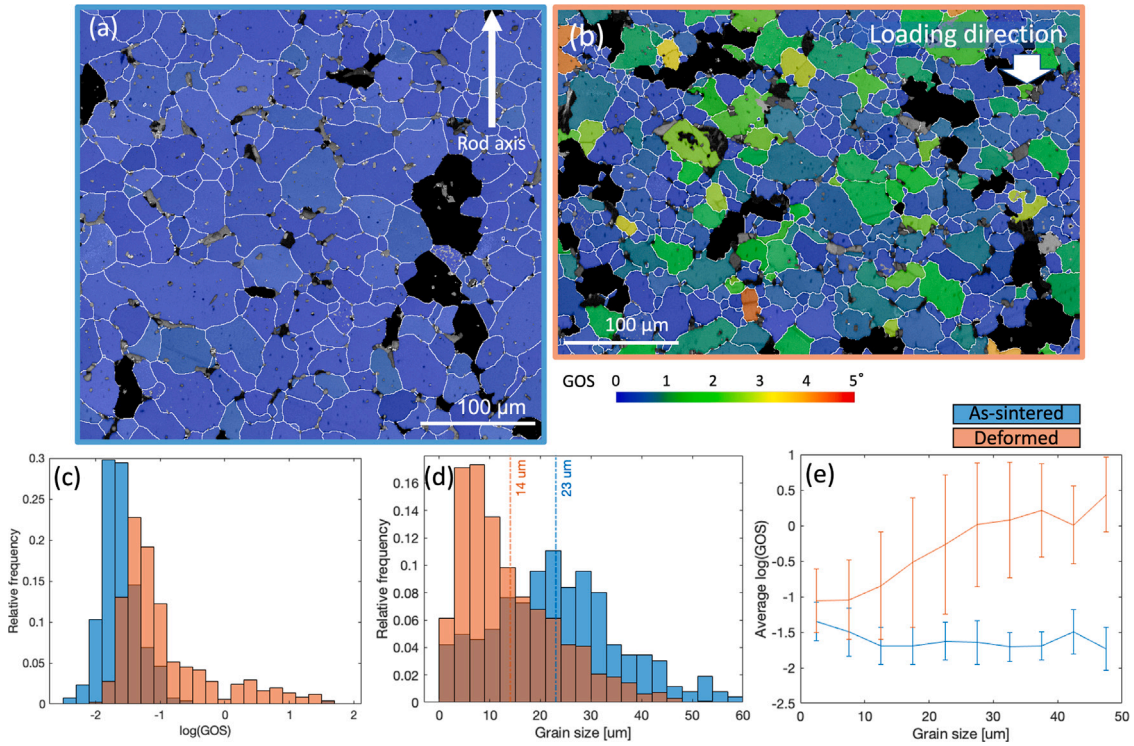

Fig. 4. GOS maps of (a) as-sintered material, and (b) deformed specimen. (c) and (d) Histograms of the logarithm of the relative frequency of GOS and grain size, respectively. (e) Average of the logarithm of GOS as a function of grain size.

expected to contribute to the pronounced stress decrease observed after the peak stress.

The deformation was not homogeneous within the grains, which can be seen from the grain reference orientation deviation map (GROD, the misorientation of each pixel relative to the average grain orientation) in Fig. 5(a). Fig. 5(b), shows the GROD map of the as-sintered material for comparison. Several grains in the deformed structure show large internal variations (corresponding to large GROD values in Fig. 4(b)) and a number of grains contain very sharp GROD gradients, as exemplified by the grain in the red square in Fig. 5(a). The kernel average misorientation (KAM, pixels in map are colour-coded based on the misorientation between the pixel and its neighbours) map in Fig. 5(c) reveals that this is due to the formation of narrow internal boundaries. In general, three different types of grains are observed in the KAM map: (1) grains with very low deformation (homogeneously blue-coloured in both the KAM and GROD maps), (2) grains in which the GROD angle varies throughout the grain (colour gradients in the GROD map and "speckled" colouring in KAM map), and (3) grains with distinct, often straight internal boundaries indicated by locally high KAM values.

A number of the grains having lines with high KAM values and/or large spread in GROD angle were analysed at higher resolution. One example is shown in Fig. 5(d). As indicated by the very sharp line in this map, the misorientation profile associated with the red line (i.e. line 2) showed a steep change in orientation (about 3°) when crossing the line, Fig. 5(e). It is believed that the line indicates a low angle grain boundary (LAGB). The misorientation of other LAGBs was in the range of about 1°–5°. No LAGBs were present in the as-sintered material and they are therefore a result of the deformation. The majority of the lines are oriented in such a way that the angle between the LAGB trace and the loading direction is large. Furthermore, the lines often, but not always, appear to be oriented parallel to the normal of the basal plane of the crystal (i.e. the [0001] c-axis), see Fig. 5(f). Large gradients

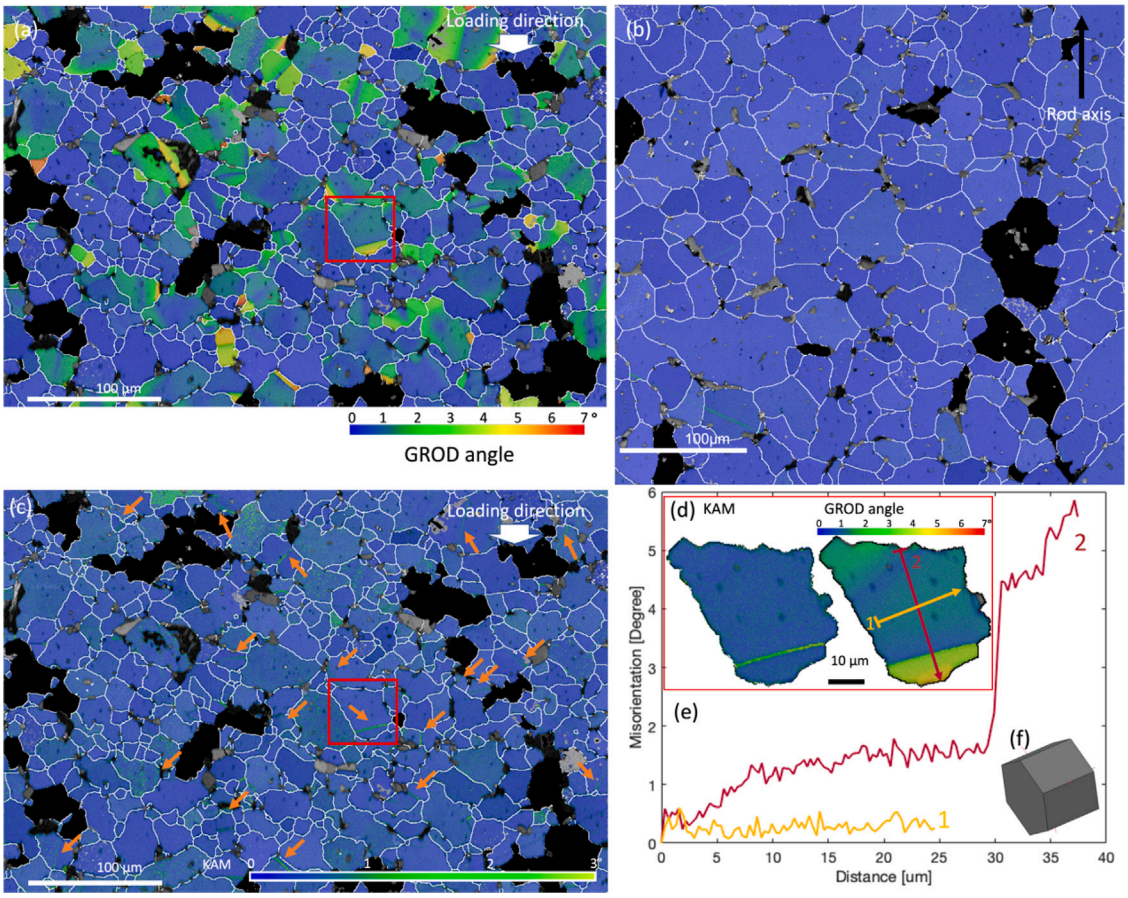

Fig. 5. (a) and (b) GROD maps of the deformed and as-sintered material, respectively. The green line present in the lower left corner of (b) is due to a scratch in the specimen from polishing. The GROD colour-bar is valid for both images. (c) KAM map of deformed specimen with a number of low angle grain boundaries indicated by arrows. (d) KAM and GROD angle map of the grain marked with a rectangle in (c). (e) Misorientation along the lines shown in (d). (f) The crystal orientation of the selected grain. (For interpretation of the references to colour in this figure legend, the reader is referred to the web version of this article.)

in the GROD values are often observed along directions normal to the [0001] direction, compare line 1 and 2 in Fig. 5(e). Due to the apparent alignment of the LAGBs with the [0001] direction, the largest GROD gradients occur normal to the LAGB traces in the maps. Line profiles showed that if no LAGB is present in the grain, the change in GROD angle (relative to the first pixel in the line) was up to 6°. However, the majority of the grains analysed had lower GROD misorientations, around 2°–3°.

However, since the EBSD data only shows a two-dimensional cross-section of the material, a detailed investigation of the orientation of the LAGBs with respect to the crystallographic orientation is not possible using this method. Hence, a thin foil sample perpendicular to the LAGB trace was prepared using FIB. The location and the orientation of the lift-out is shown in Fig. 6(a). The LAGB is running, with a small curvature, from the top (the surface plane in 6(a)) to the bottom of the liftout, see KAM map in Fig. 6(b). In addition to the change in crystal orientation attributed to the LAGB itself, the orientation also varies in the region close to the LAGB, which can bee seen in the GROD map in Fig. 6(c). Fig. 6(d) shows a STEM BF image corresponding to Fig. 6(b) and (c). The LAGB appears very sharp, and the grain interior contains multiple individual dislocations. Interestingly, a second curved boundary associated with the other side of the region with a GROD gradient appears to be present indicated by white arrows in Fig. 6(c) and (d), but this is less well defined and not visible in the KAM map. We also note the presence of several nano-scale Al_2O_3 particles inside the grains, as previously mentioned, and a larger particle which is only visible in the STEM image as it is located on the back side of the thin foil when oriented for EBSD. Both the small and large

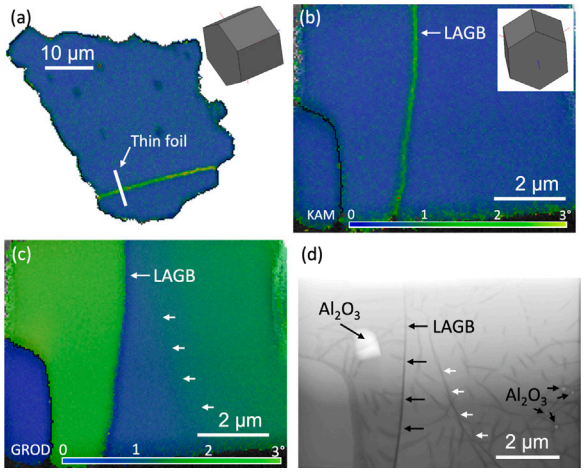

Fig. 6. (a) Location of the thin foil lift-out. (b) KAM and (c) GROD maps of the thin foil. The schematic unit cells in (a) and (b) visually show the crystal orientations with the respect to the image plane. (d) STEM BF image showing the LAGB and dislocations in the grain interior. The Al_2O_3 particles in (d) are not visible in (b) and (c) because of the shallow interaction depth of EBSD.

particles appear to have an effect on the plastic deformation, as a large number of dislocations are seen in their vicinity. This indicates a potential particle strengthening contribution from the presence of the intragranular Al_2O_3 particles, which could also act to limit recovery.

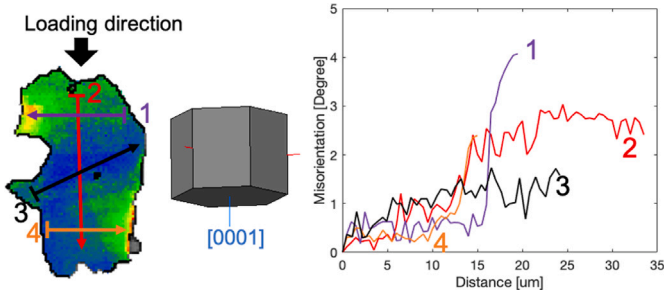

Fig. 7. A grain oriented with the [0001] close to the loading direction, with misorientation profiles of the four lines indicated in GROD angle map.

Fig. 7 shows an example of a grain without LAGB, where the GROD distribution is considerably more complex. Again, the largest gradients are observed perpendicular to the [0001] direction, but the lattice rotation is concentrated in two opposing "corners" of the grain. The particular grain was oriented in with the [0001] axis almost parallel to the loading direction, and hence has a very low Schmid factor (0.01) for the $\langle 2\bar{1}\bar{1}0\rangle(0001)$ slip system. The areas having large GROD gradients indicate regions with relatively high GND density, and pore formation (and later crack initiation) is likely to be associated with such concentrations. However, as mentioned above, only a modest increase in the volume fraction of pores, from around 1 vol. % to approximately 3 vol. %, was observed, and no cracks were detected at the strain levels in the present study.

4. Discussion

The EBSD investigation in the present study shows that the material has not been deformed homogeneously. Some grains were much more deformed than others, as revealed by the KAM, GOS and GROD maps in Figs. 4 and 5. Similar phenomenon has been reported by Mitra et al., in the case of polycrystalline $MoSi_2$ with the $C11_b$ structure [19], where it was argued that grains which had slip systems with a low critical resolved shear stress favourably oriented with respect to the loading axis were more prone to deform than other grains. In the case of uniaxially compressed $Mo(Si,Al)_2$ single crystals only one slip system, $\langle 2\bar{1}\bar{1}0\rangle(0001)$, has been found. Furthermore, Inui et al. [6] have shown that the deformation is very orientation dependent and that single crystals loaded along the [0001] or $\{1\bar{2}10\}$ direction fracture without any plastic deformation at all, even at temperatures as high as 1500 °C [6]. In the present investigation the majority of the grains with low Schmid factor for $\langle 2\bar{1}\bar{1}0\rangle(0001)$ slip had low deformation (GOS value), which agrees with previous reports. However, some grains oriented with the [0001] axis close to (less than 10° away from) the loading direction, were indeed plastically deformed despite the Schmid factor being close to zero. This would suggest that the elastic interactions with surrounding grains impose a stress state with a significant shear component on the $\langle 2\bar{1}\bar{1}0\rangle(0001)$ slip system (as discussed before), or that additional slip systems are activated. The activation of additional slip systems in the presence of complex stress states has been reported for C40 $NbSi_2$ [20], which otherwise nominally has the same single slip system as $Mo(Si,Al)_2$ and the other C40 silicides [9,12]. While $\langle 2\bar{1}\bar{1}0\rangle(0001)$ slip occurred in the homogeneously deformed volumes of $NbSi_2$ single crystals tested in tension at elevated temperature, four new slip systems ($\langle 1\bar{2}10\rangle\{10\bar{1}0\}$, $\langle 1\bar{2}10\rangle\{10\bar{1}1\}$, $\langle 0001\rangle\{10\bar{1}0\}$ and $\langle 11\bar{2}X\rangle\{11\bar{2}Y\}$, where (X×Y) = −6) were found to be operative in the vicinity of the main crack to accommodate local stress concentrations and multiaxial stress states [20]. Elastic interactions between adjacent grains due to strain compatibility give rise to very complex local stress states during deformation of polycrystalline materials, and hence it is indeed possible that non-dominating slip systems may become active also in $Mo(Si,Al)_2$ in the present case.

The deformation did not only differ from grain to grain, but also within the deformed grains. From the two-dimensional cross sections investigated using EBSD, it was observed that the direction of the largest orientation gradient often followed a certain crystallographic direction in each grain, i.e. perpendicular to the [0001] axis. In grains where LAGBs have been formed (as exemplified in Fig. 5(d) and (e)), the trace of this boundary is typically aligned with the [0001] direction, and the orientation gradient is perpendicular to the LAGB trace. The change in misorientation parallel to the LAGB trace was often very low, typically less than 0.5° (i.e. in principle at the noise level) across the entire grain width. There are also exceptions to this, where more complex deformation fields are observed, where Fig. 7 provides a prominent example. However, even in such grains the largest misorientation gradients were observed perpendicular to [0001]. The larger gradients along [0001] is a result of the different gradients perpendicular to [0001] in different parts of the grains. Mitra et al. [19] observed LAGBs in individual grains in $C11_b$ $MoSi_2$, and suggested that their formation was a dynamic recovery mechanism. If this is the case, there would likely exist a "critical deformation level" where LAGB formation becomes energetically favourable. Indeed, we do find that grains having a larger misorientation spread (typically above 4°) often contains LAGBs.

In spite of the presence of LAGBs, which according to Mitra et al. [19] will contribute to dynamic recovery through the emission and absorption of dislocations, the number of grains containing such boundaries is small. Given the very pronounced stress decrease observed after the maximum stress in Fig. 2, it is therefore unlikely that LAGB formation alone is responsible for the softening. In the present work we find a relatively large fraction of small grains with very low level of deformation (GOS) after compression (see Fig. 4(d) and (e)), which suggests the occurrence of extensive DRX. Mitra et al. [19] did not report any evidences of DRX in $MoSi_2$, but it has been observed by Hardwick et al. [21] in polycrystalline $MoSi_2$ deformed by compression to a high strain (57%) at a strain rate of 10^{-4} s^{-1} at 1300 °C. It was argued that DRX would only occur in microstructures where grain boundary sliding was not the dominating deformation mechanics. Furthermore, the window for DRX in terms of temperature and strain rates was found to be quite narrow. Deformation at temperatures above 1400 °C produced grain growth, whereas lower temperatures (or higher strain rates) increased the proportion of microcracking, leading to less dislocation accumulation and thus suppression of DRX [21]. Here we show that DRX readily occurs in polycrystalline $Mo(Si,Al)_2$ deformed at 1300 °C at a strain rate of 10^{-4} s^{-1}, and that suggests that this has a large impact on the stress evolution and deformation mechanisms during hot deformation. However, it is not yet confirmed if DRX is the dominating mechanism leading to the observed softening of polycrystalline $Mo(Si,Al)_2$. As the stress levels towards the end of the tests are significantly lower than the initial yield stress, which would not be expected for a material where DRX is the dominating relaxation mechanisms, it is likely that other phenomena, such as grain boundary sliding (not present in single crystalline materials), contribute to the softening. It is possible that Joule heating, which gives rise to an uneven heating of the material with higher temperatures at grain boundaries [22–24], triggers grain boundary sliding. Furthermore, the fine microstructure formed due to DRX may in itself enhance grain boundary sliding [19]. This clearly calls for further studies to identify both the window for DRX and the temperature and strain rate dependent critical strain and kinetics, as well as the deformation mechanisms. Furthermore, for metallic materials it has been shown that DRX is accelerated during hot compression using Joule heating compared to identical processing using a conventional furnace [25]. This may be one reason for discrepancies in observations of DRX between hot compression studies also in the case of ceramics like $MoSi_2$, and contribute to difficulties in establishing DRX strain rate/temperature windows. However, in the present case it provides relevant conditions since the intended application for the studied material is resistive heating elements.

5. Conclusions

We present the first detailed report of stress–strain response and microstructure of deformed polycrystalline C40 structured $Mo(Si,Al)_2$, and indeed of any polycrystalline C40 transition metal silicide, to our knowledge. Samples were compressed at a strain rate of 10^{-4} s^{-1} at 1300 °C, and subsequently investigated using EBSD. The results can be summarized in the following points:

1. The polycrystalline samples were readily deformed to strains above 10% with only a modest increase in porosity and no observable crack formation, in spite of nominally possessing only a single slip system. The maximum stress during deformation agrees well with previous studies. After the maximum stress a pronounced softening is observed, which has not been previously reported.
2. The deformation is inhomogeneous both on the intragranular and intergranular scale. Grains with low Schmid factor generally exhibited less deformation, although prominent exceptions to this occurred. Very complex deformation fields were observed, but in general largest misorientation gradients were aligned perpendicular to the [0001] direction. The ability to undergo large scale plastic deformation without cracking and to accommodate the complex deformation fields presented suggest that the triaxial stress states generated in the grains by the elastic intergranular interactions could promote activation of additional slip systems. Such slip systems have been observed in C40 structured $NbSi_2$ in the vicinity of cracks, which also induce highly complex stress states.
3. Low angle grain boundaries formed in highly deformed grains, which probably contributed to the softening through dynamic recovery. Even more pronounced was the occurrence of dynamic recrystallization, leading to the formation of a large fraction of small undeformed grains. However, it is unlikely that relaxation due to combined of LAGB formation and DRX can fully explain the softening to stress levels far below the initial yield strength of the material.

These results indicate that the existing knowledge of the mechanical behaviour of C40 structured silicides based on results from tests of single crystals cannot be directly extrapolated to polycrystals. Further investigations into both slip system activity and occurrence/kinetics of DRX in polycrystalline C40 transition metal silicides can reveal generic and system specific behaviours and their origins. In particular, comparison between systems deforming through synchroshear ($Mo(Si,Al)_2$ and $CrSi_2$) and conventional shear ($NbSi_2$, VSi_2 and $TaSi_2$), would be of great interest. We also note that clarifying the above points is particularly important for $Mo(Si,Al)_2$, as the high temperature mechanical behaviour is likely to become very important for electrification of industrial heating processes and thereby the transition to sustainable manufacturing methods.

CRediT authorship contribution statement

Aina Edgren: Conceptualization, Methodology, Investigation, Writing – original draft, Visualization. **Erik Ström:** Supervision, Conceptualization, Resources, Writing – review & editing. **Ren Qiu:** Investigation. **Lars Frisk:** Investigation, Resources. **Farid Akhtar:** Investigation, Resources, Writing – review & editing. **Magnus Hörnqvist Colliander:** Supervision, Conceptualization, Writing – review & editing, Funding acquisition, Project administration.

Declaration of competing interest

One or more of the authors of this paper have disclosed potential or pertinent conflicts of interest, which may include receipt of payment, either direct or indirect, institutional support, or association with an entity in the biomedical field which may be perceived to have potential conflict of interest with this work. For full disclosure statements refer to https://doi.org/10.1016/j.msea.2022.143387.

Aina Edgren and Erik Ström are employees of Kanthal AB, a manufacturer of commercial heating elements.

Data availability

The data that support the findings of this study are available from the corresponding author upon reasonable request.

Acknowledgements

This research was funded by the Swedish Foundation for Strategic Research (SSF) and Kanthal AB, through the industrial Ph.D. student grant ID18-0064. The work was performed in part at Chalmers Materials Analysis Laboratory (CMAL).

References

[1] S. Madeddu, F. Ueckerdt, M. Pehl, J. Peterseim, M. Lord, K.A. Kumar, C. Krüger, G. Luderer, The CO_2 reduction potential for the European industry via direct electrification of heat supply (power-to-heat), Environ. Res. Lett. 15 (2020).
[2] M. Halvarsson, T. Jonsson, L. Ingemarsson, M. Sundberg, J.E. Svensson, L.G. Johansson, Microstructural investigation of the initial oxidation at 1450 °C and 1500 °C of a $Mo(Si,Al)_2$-based composite, Mater. High Temp. 26 (2009) 137–143.
[3] L. Ingemarsson, K. Hellström, L.G. Johansson, J.E. Svensson, M. Halvarsson, Oxidation behaviour of a $Mo(Si,Al)_2$ based composite at 1500 °C, Intermetallics 19 (2011) 1319–1329.
[4] L. Ingemarsson, K. Hellström, S. Canovic, T. Jonsson, M. Halvarsson, L.G. Johansson, J.E. Svensson, Oxidation behavior of a $Mo(Si,Al)_2$ composite at 900-1600 °C in dry air, J. Mater. Sci. 48 (2013) 1511–1523.
[5] L. Ingemarsson, M. Halvarsson, J. Engkvist, T. Jonsson, K. Hellström, L.G. Johansson, J.E. Svensson, Oxidation behavior of a $Mo(Si,Al)_2$-based composite at 300-1000 °C, Intermetallics 18 (2010) 633–640.
[6] H. Inui, M. Moriwaki, K. Ito, M. Yamaguchi, Plastic deformation of single crystals of $Mo(Si, Al)_2$ with the C40 structure, Phil. Mag. A 77 (1998) 375–394.
[7] H. Inui, K. Ishikawa, M. Yamaguchi, Effects of alloying elements on plastic deformation of single crystals of $MoSi_2$, Intermetallics 8 (2000) 1131–1145.
[8] H. Inui, M. Moriwaki, S. Ando, M. Yamaguchi, Plastic deformation of single crystals of $CrSi_2$ with the C40 structure, Mater. Sci. Eng. A 239–240 (1997) 63–68.
[9] M. Moriwaki, K. Ito, H. Inui, M. Yamaguchi, Plastic deformation of single crystals of $NbSi_2$ with the C40 structure, Mater. Sci. Eng. A 239–240 (1997) 69–74.
[10] H. Inui, M. Moriwaki, M. Yamaguchi, Plastic deformation of single crystals of VSi_2 and $TaSi_2$ with the C40 structure, Intermetallics 6 (1998) 723–728.
[11] T. Nakano, M. Kishimoto, D. Furuta, Y. Umakoshi, Effect of substitutional elements on plastic deformation behaviour of $NbSi_2$-based silicide single crystals with C40 structure, Acta Mater. 48 (2000) 3465–3475.
[12] H. Inui, M. Yamaguchi, Deformation mechanisms of transition-metal disilicides with the hexagonal C40 structure, Intermetallics 9 (2001) 857–862.
[13] Y. Umakoshi, T. Nakano, K. Kishimoto, D. Furuta, K. Hagihara, M. Azuma, Strength and deformation mechanism of C40-based single crystal and polycrystalline silicides, Mater. Sci. Eng. A 261 (1999) 113–121.
[14] K. Hagihara, T. Nakano, Y. Umakoshi, Mechanical properties of C40-based ternary $Mo(Si,Al)_2$ and quaternary $(Mo,Zr)(Si,Al)_2$ silicides, Scr. Mater. 38 (1998) 471–476.
[15] R. Mitra, N.E. Prasad, S. Kumari, A.V. Rao, High-temperature deformation behavior of coarse- and fine-grained MoSi 2 with different silica contents, 2014.
[16] E. Eriksson, J. Andersson, M. Hörnqvist Colliander, The effect of grain boundary carbides on dynamic recrystallization during hot compression of Ni-based superalloy haynes 282 TM, Metall. Mater. Trans. A 53 (2022) 29–38.
[17] D.J. Yu, D.S. Xu, H. Wang, Z.B. Zhao, G.Z. Wei, R. Yang, Refining constitutive relation by integration of finite element simulations and Gleeble experiments, J. Mater. Sci. Technol. 35 (2019) 1039–1043.
[18] T. Gao, L. Ma, X.-G. Peng, Study on temperature distribution of specimens tested on the gleeble 3800 at hot forming conditions, J. Electron. Sci. Technol. 12 (2014) 419–423.

[19] R. Mitra, N.E. Prasad, S. Kumari, A.V. Rao, High-temperature deformation behavior of coarse- and fine-grained $MoSi_2$ with different silica contents, Metall. Mater. Trans. A 34 A (2003) 1069–1088.
[20] T. Nakano, M. Azuma, Y. Umakoshi, Tensile deformation and fracture behaviour in $NbSi_2$ and $MoSi_2$ single crystals, Acta Mater. 50 (2002) 3731–3742.
[21] D.A. Hardwick, P.L. Martin, Microcracking, strain rate and large strain deformation effects in molybdenum disilicide, in: MRS Proceedings: Silicides and Refractory Metals, 1993.
[22] B.J. Ruszkiewicz, L. Mears, J.T. Roth, Investigation of heterogeneous Joule heating as the explanation for the transient electroplastic stress drop in pulsed tension of 7075-T6 aluminum, Trans. ASME, J. Manuf. Sci. Eng. 140 (2018) 1–11.
[23] A. Majumdar, J.P. Carrejo, J. Lai, Thermal imaging using the atomic force microscope, Appl. Phys. Lett. 62 (1993) 2501–2503.
[24] R. Fan, J. Magargee, P. Hu, J. Cao, Influence of grain size and grain boundaries on the thermal and mechanical behavior of 70/30 brass under electrically-assisted deformation, Mater. Sci. Eng. A 574 (2013) 218–225.
[25] A. Nicolaÿ, J.M. Franchet, J. Cormier, R.E. Logé, G. Fiorucci, J. Fausty, M. Van Der Meer, N. Bozzolo, Influence of Joule effect heating on recrystallization phenomena in Inconel 718, Metall. Mater. Trans. A 52 (2021) 4572–4596.